Impact of poroelastic effects on the inversion of fracture properties from AVOAz data in HTI media

Nicolás D. Barbosa[1], Corinna Köpke[2,3], Eva Caspari[2], J. Germán Rubino[4], James Irving[2], and Klaus Holliger[2,5]

(November 22, 2019)

Running head: **WIFF effects on AVOAz data**

ABSTRACT

The identification and characterisation of fractures is an important objective in many areas of Earth and Environmental Sciences. Amplitude versus offset and azimuth (AVOAz) analysis of seismic reflection data is a key method for achieving these tasks. Theoretical and experimental studies have shown that the presence of pore fluids together with the strong mechanical contrast between the fractures and their embedding background give rise to ~~fluid pressure diffusion~~ wave-induced fluid flow (WIFF) effects. This implies that the effective stiffness tensor of a fluid-saturated fractured rock defining its seismic response becomes viscoelastic and frequency-dependent. In spite of this, AVOAz analysis typically relies on end-member-type elastic stiffness models that either assume a relaxed (i.e., equilibrated)

[1]Department of Earth Sciences, University of Geneva, Geneva, Switzerland

[2]Applied and Environmental Geophysics Group, Institute of Earth Sciences, University of Lausanne, Lausanne, Switzerland

[3]Now at: German Aerospace Center, Institute for the Protection of Maritime Infrastructures, Bremerhaven, Germany

[4]CONICET, Centro Atómico Bariloche - CNEA, San Carlos de Bariloche, Argentina

[5]School of Earth Sciences, Zhejiang University, Hangzhou, China

or unrelaxed (i.e., unequilibrated) state of the wave-induced fluid pressure in the rock. In general, however, neither the appropriateness of the chosen model nor the associated errors in the inversion process are known. To shed some light onto this topic, we consider a poroelastic medium containing parallel vertical fractures and generate synthetic seismic AVOAz data using Rüger's (1998) approximations for PP-wave reflection coefficients in Horizontally Transversely Isotropic media. A Markov-chain-Monte-Carlo method is used to perform a Bayesian inversion of the synthetic seismic AVOAz data. We quantify the influence of WIFF effects on the AVOAz inversion results when elastic relaxed and unrelaxed models are used as forward solvers of inversion schemes to estimate the fracture volume fraction, the elastic moduli, and the porosity of the background rock, as well as the overall weakness of the medium due to the presence of fractures. Our results indicate that, when dealing with single-frequency data, relaxed elastic models provide biased but overall better inversion results than unrelaxed ones, for which some fracture parameters cannot be resolved. An improved inversion performance is achieved when using frequency-dependent data, which illustrates the importance of accounting for poroelastic effects.

INTRODUCTION

The identification, location, and characterisation of fractures receive great interest due to their impact on the mechanical and hydraulic properties of the affected rock volumes. Geophysical techniques in general and seismic methods in particular have been extensively used as non-invasive means to locate fractures and to characterise their properties (e.g., National Research Council, 1996; Liu and Martinez, 2013). Probably the most remarkable manifestation of the presence of fractures embedded in an otherwise isotropic background is the effective anisotropic behavior of seismic waves. This has made the analysis of reflection amplitude variations with offset and azimuth (AVOAz) a common and successful practice for retrieving practically important parameters of the fractured formation such as, for example, the density and the azimuthal orientation of the fractures, as well as the type of saturating pore fluid (e.g., Bakulin et al., 2000; Shen et al., 2002; Fang et al., 2016).

Seismic waves propagating in fluid-saturated fractured rocks experience attenuation and velocity dispersion caused by a mechanism broadly known as wave-induced fluid flow (WIFF). The strong mechanical contrast between the compliant fractures and the much stiffer embedding background favours the development of fluid pressure gradients between these regions in response to the deformation imposed by a propagating seismic wave. The internal friction that is associated with the fluid pressure equilibration process then manifests itself in the form of seismic attenuation and velocity dispersion. Mesoscopic WIFF, which occurs due to the presence of fractures on a scale much larger than the pore size but much smaller than the prevailing wavelength, is considered to be a significant source of seismic energy dissipation in the seismic frequency band (e.g., Müller et al., 2010). Fig. 1 illustrates the frequency dependence of the P-wave modulus (Fig. 1a) and the attenuation

(Fig. 1b) normal to a set of parallel fractures. The frequencies in Fig. 1 are normalised with respect to the characteristic frequency at which the attenuation and modulus dispersion due to mesoscopic WIFF are maximal. This illustrates that, in the presence of WIFF, the anisotropic behavior of the medium also becomes frequency-dependent. The dependence of the mesoscopic WIFF mechanism on the rock physical properties, the fracture geometry, and the frequency makes the analysis of frequency-dependent seismic attributes a valuable source of information with regard to the mechanical and hydraulic properties (e.g., Al-Harrasi et al., 2011; Tillotson et al., 2011; Ali and Jakobsen, 2014).

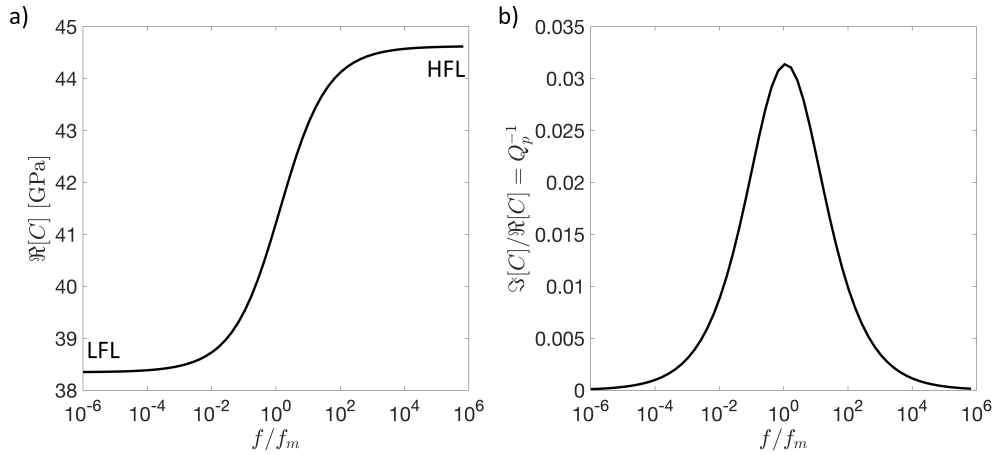

Figure 1: (a) P-wave modulus dispersion and (b) inverse quality factor normal to a set of parallel fractures as functions of the frequency normalised with respect to the mesoscopic WIFF characteristic frequency f_m. LFL and HFL refer to the low- and high-frequency limits of the P-wave modulus, respectively. The physical properties used to compute the complex-valued P-wave modulus C are given in Table 1.

Despite the potential value of a frequency-dependent analysis, the AVOAz interpretation of seismic data typically relies on the low- or high-frequency limits of the underlying

frequency-dependent models (e.g., Rathore et al., 1995; Rüger, 2002; Chen et al., 2017). Relaxed or low-frequency models (e.g., Thomsen, 1995) assume that the permeability is sufficiently high to ensure that, at the prevailing frequencies, both the fractures and their background are in fluid pressure equilibrium during the passage of the seismic wave. This limit is denoted in Fig. 1 as LFL and is consistent with the well-known Gassmann (1951) equations. Conversely, unrelaxed or high-frequency models (e.g., Hudson, 1980) are used when the permeability is assumed to be sufficiently low such that there is not enough time for fluid pressure communication between the fractures and the background during a seismic wave cycle (HFL in Fig. 1). That is, the fractures behave as being hydraulically isolated from their embedding background. Bakulin et al. (2000) performed a comprehensive analysis of inversion performance to obtain fluid-saturated fracture properties from AVO data considering Thomsen's (1995) and Hudson's (1980) limiting models. It is expected that, in the presence of significant WIFF effects, the physical and geometrical properties estimated using these limiting models are not accurate. Indeed, Bakulin et al. (2000) pointed out that, in the presence of WIFF effects, the interpretation of fracture properties estimated using limiting elastic models may be ambiguous without additional information. In this work, we address this question for the case of a medium containing a set of parallel fractures. Despite its simplicity, this model can be regarded as a first-order approximation of many reservoirs exhibiting a predominant direction of minimum compressive stress. In this scenario, open fractures will tend to align perpendicular to the smallest compressive stress, which is usually horizontal (Liu and Martinez, 2013).

A set of parallel fractures produces effective transverse anisotropy with a single axis of symmetry. The frequency-dependent stiffness matrix describing the seismic response of such a medium is a function of the porosity, the permeability, the pore fluid properties,

and the elastic moduli, as well as of the geometry, the mechanical properties, and the distribution of the fractures. In general, the two classical representations used to model the seismic effects of a set of parallel fractures are inclusions (e.g. Hudson, 1980) and linear slip boundary interfaces (Schoenberg, 1980). The theoretical model developed by Chapman (2003) is arguably the most extensively used approach for fracture parameter inversion using frequency-dependent seismic anisotropy data (e.g., Maultzsch et al., 2003; Chapman et al., 2006; Maultzsch et al., 2007; Tillotson et al., 2014). This inclusion-based model takes into account the fluid-pressure relaxation process between the pore space of the background medium and the fluid-filled mesoscopic fractures. A drawback of utilising the model of Chapman (2003) is that it requires an estimation of the characteristic relaxation time of the fluid-pressure diffusion process, which is inversely proportional to f_m (Fig. 1). Given that this parameter is difficult to measure, it is generally estimated from a known characteristic relaxation time of a rock sample through a calibration process, which assumes that the relaxation time is proportional to the ratio between the fluid viscosity and the permeability (e.g., Al-Harrasi et al., 2011). The linear slip model, on the other hand, assumes that the effective compliance of the fractured medium can be computed as the sum of the excess compliance due to the presence of fractures and the compliance of the background medium. Brajanovski et al. (2005) used the linear slip theory (LST) to derive the frequency-dependent anisotropic seismic response of a distribution of parallel fluid-saturated fractures, represented as a limiting case of infinitely thin and compliant porous layers embedded in a less porous and stiffer background. Recently, Guo et al. (2017a,b) showed that the inherently small but finite aperture of fractures can produce significant departures in the seismic response of fractured media with respect to the interface-fracture model of Brajanovski et al. (2005).

The goal of this work is two-fold. First, we explore the impact of neglecting the frequency dependence of the effective anisotropy of fractured media when performing inversion of AVOAz data. To do so, we create synthetic AVOAz data using the planar-fracture model of Guo et al. (2017a), which accounts for the finite aperture of fractures and is valid for fractures with radii much larger than the prevailing seismic wavelengths (Gurevich et al., 2009). Then, we employ the typically used relaxed and unrelaxed elastic models as forward solvers in the inversion procedure. In order to examine the inversion performance of different models and their robustness, we follow a Bayesian approach. In a second step, we explore the potential benefits of considering frequency-dependent data in the inversion. It is important to mention that outlining the processing of seismic data for making them amenable to AVOAz analysis is beyond the scope of this study. Downton (2005) provides a comprehensive description of the processing sequence as well as of the factors related to data collection, wave propagation effects, and data processing that may affect the quality of an AVOAz data set.

FORWARD PROBLEM

Effective properties of fluid-saturated fractured rocks

A set of parallel fractures produces effective transverse isotropy with a single axis of symmetry normal to the fracture planes. Assuming that the symmetry axis is parallel to the x-axis,

the relation between the stress τ_{ij} and strain ε_{ij} components in the fractured medium is

$$\begin{bmatrix} \tau_{xx} \\ \tau_{yy} \\ \tau_{zz} \\ \tau_{yz} \\ \tau_{xz} \\ \tau_{xy} \end{bmatrix} = \begin{bmatrix} C_{11} & C_{12} & C_{12} & 0 & 0 & 0 \\ C_{12} & C_{22} & C_{23} & 0 & 0 & 0 \\ C_{12} & C_{23} & C_{22} & 0 & 0 & 0 \\ 0 & 0 & 0 & (C_{22}-C_{23})/2 & 0 & 0 \\ 0 & 0 & 0 & 0 & C_{55} & 0 \\ 0 & 0 & 0 & 0 & 0 & C_{55} \end{bmatrix} \cdot \begin{bmatrix} \varepsilon_{xx} \\ \varepsilon_{yy} \\ \varepsilon_{zz} \\ 2\varepsilon_{yz} \\ 2\varepsilon_{xz} \\ 2\varepsilon_{xy} \end{bmatrix}, \tag{1}$$

where the stiffness coefficients C_{ij} contain all the information about the fractured rock that describes its effective anisotropic seismic response.

Under dry conditions, a common approach to compute the stiffness matrix (Eq. 1) is following the LST formulation. In that case, the stiffness matrix of a dry fractured rock $\mathbf{C}^{\text{dry}}$ can be estimated as (Schoenberg and Douma, 1988)

$$\mathbf{C}^{\text{dry}} = (\mathbf{S}^{\text{dry}})^{-1} = (\mathbf{S}_b^{\text{dry}} + \mathbf{Z}^{\text{dry}})^{-1}, \tag{2}$$

where $\mathbf{S}^{\text{dry}}$ and $\mathbf{S}_b^{\text{dry}}$ are the compliance tensors of the dry fractured rock and the dry background medium, respectively. For a set of rotationally invariant fractures whose normal is parallel to the x-axis, the dry fracture excess compliance $\mathbf{Z}^{\text{dry}}$ is approximated as (Schoenberg and Sayers, 1995)

$$\mathbf{Z}^{\text{dry}} = \begin{bmatrix} Z_N & 0 & 0 & 0 & 0 & 0 \\ 0 & 0 & 0 & 0 & 0 & 0 \\ 0 & 0 & 0 & 0 & 0 & 0 \\ 0 & 0 & 0 & 0 & 0 & 0 \\ 0 & 0 & 0 & 0 & Z_T & 0 \\ 0 & 0 & 0 & 0 & 0 & Z_T \end{bmatrix}, \tag{3}$$

where Z_N and Z_T are the dry normal and tangential compliances, respectively. The excess compliance predicted by the LST is similar to that produced by a set of parallel poroelastic thin-layers having appropriate infilling material, which can be obtained as (Brajanovski et al., 2005)

$$\begin{aligned} L &= \frac{V_f}{Z_N}, \\ \mu_m &= \frac{V_f}{Z_T}, \end{aligned} \tag{4}$$

where V_f is the fracture volume fraction and L and μ_m are the dry P-wave and shear moduli of the fracture infill material, respectively.

Under fluid-saturated conditions, the stiffness matrix in Eq. 1 becomes complex-valued and frequency-dependent. Guo et al. (2017a,b) propose an analytical model to compute the C_{ij} coefficients representing a fluid-saturated medium containing a distribution of parallel fractures. This model relies on a poroelastic representation of the fractured medium as in Brajanovski et al. (2005) and Gurevich et al. (2009). One of the assumptions of the model of Guo et al. (2017a,b) is that, regardless of the direction of wave propagation, the fluid pressure diffusion between the fractures and the background is predominantly normal to the surface of the fractures (e.g. Krzikalla and Müller, 2011; Barbosa et al., 2018). As a consequence, the frequency dependence of the stiffness coefficients C_{ij} can be quantified by a single relaxation function. Gurevich et al. (2009) showed that for a random distribution of fractures this frequency dependence can be described as

$$\frac{1}{C_{ij}(\omega)} = \frac{1}{C_{ij}^u} + \left(\frac{1}{C_{ij}^u} - \frac{1}{C_{ij}^r}\right)/(1 + \sqrt{-i\omega\tau}), \tag{5}$$

with C_{ij}^r and C_{ij}^u being the low- and high-frequency limits of $C_{ij}(\omega)$, respectively, and ω the angular frequency. These two sets of stiffness coefficients represent the effective properties of the fractured medium for the two limiting elastic models. τ is the characteristic time of the fluid pressure diffusion process which, due to its uni-directional nature, is the same as

that for the P-wave modulus in the direction perpendicular to the fracture planes. Hence, τ can be computed as (Guo et al., 2017a)

$$\tau = \left(\frac{C_{11}^u - C_{11}^r}{C_{11}^r G} \right)^2, \tag{6}$$

and

$$G = \frac{\frac{2}{H} C_{11}^u \left(\frac{\alpha_b M_b}{C_b} - \frac{\alpha_f M_f}{C_f} \right)^2}{\sqrt{\frac{M_b L_b \eta}{C_b \kappa_b}} + \sqrt{\frac{M_f L_f \eta}{C_f \kappa_f}}}. \tag{7}$$

In Eq. 7, the subscripts b and f refer to background and fracture properties, respectively. Moreover, $L = K_m + 4\mu_m/3$ and $C = L + \alpha^2 M$ are the dry and saturated P-wave moduli, with K_m denoting the dry frame bulk modulus. The equivalent elastic moduli of the poroelastic material filling the fractures can be obtained using Eq. 4. The Biot-Willis effective stress coefficient α and Biot's fluid-storage modulus M are defined as

$$\begin{aligned} \alpha &= 1 - K_m/K_s, \\ M &= \left(\frac{\alpha - \phi}{K_s} + \frac{\phi}{K_{fl}} \right)^{-1}, \end{aligned} \tag{8}$$

where ϕ is the porosity, K_{fl} and K_s the bulk moduli of the fluid phase and the solid grains, respectively, κ the permeability, η the viscosity of the saturating fluid, and H the inverse of the fracture intensity.

The details of the computation of the coefficients C_{ij}^r and C_{ij}^u involved in Eq. 5 for a medium containing a distribution of parallel fractures are given in Appendix A. It is important to mention that computing the corresponding relaxed and unrelaxed limits (Eqs. A-1 and A-5, respectively) requires knowledge of the effective properties under dry conditions (Eq. 2).

AVOAz model

A seismic wave incident at a boundary between two anisotropic media can generate reflected quasi-P-waves and quasi-S-waves as well as transmitted quasi- P-waves and quasi-S-waves. In general, the reflection and transmission coefficients vary with the direction of incidence. This is important because the AVOAz characteristics can be detected and quantified through 3D seismic surveys, which makes it a popular seismic attribute for reservoir characterisation (e.g., Mavko et al., 2009). In this work, we use PP-wave reflection coefficient data corresponding to an interface separating an isotropic medium overlying an anisotropic fractured medium (Fig. 2). Given that the minimum in-situ compressive stress in reservoirs is typically horizontal (Liu and Martinez, 2013), we assume that fractures in the lower medium are vertical. Hence, the lower medium is characterised by horizontal transverse isotropy (HTI) and we set the x-axis to be parallel to the symmetry axis of the fractures (Fig. 2).

Assuming weakly anisotropic media, Rüger (1998) found that the PP-wave reflection coefficients at the interface separating two HTI media with the same orientation of the symmetry axis can be approximated as

$$\begin{aligned} R_{PP}(\theta,\zeta) = \frac{\Delta Z}{2\bar{Z}} + \frac{1}{2}\Bigg[\frac{\Delta\alpha}{\bar{\alpha}} - \left(\frac{2\bar{\beta}}{\bar{\alpha}}\right)^2\frac{\Delta G}{\bar{G}} + \\ \left(\Delta\delta^V + 2\left(\frac{2\bar{\beta}}{\bar{\alpha}}\right)^2\Delta\gamma\right)\cos^2(\zeta)\Bigg]\sin^2(\theta) + \\ \frac{1}{2}\left[\frac{\Delta\alpha}{\bar{\alpha}} + \Delta\varepsilon\cos^4(\zeta) + \Delta\delta^V\sin^2(\zeta)\cos^2(\zeta)\right]\sin^2(\theta)\tan^2(\theta), \end{aligned} \tag{9}$$

where θ is the incidence angle and ζ is the azimuth defined with respect to the symmetry axis normal to the fractures. In addition, we have

$$\begin{aligned} &\alpha = \sqrt{\frac{C_{33}}{\rho}}, \quad \beta = \sqrt{\frac{C_{44}}{\rho}}, \quad G = C_{44}, \quad Z = \alpha\rho, \quad \varepsilon = \frac{C_{11}-C_{33}}{2C_{33}}, \\ &\delta^V = \frac{(C_{13}+C_{55})^2 - (C_{33}-C_{55})^2}{2C_{33}(C_{33}-C_{55})}, \quad \gamma = \frac{C_{66}-C_{44}}{2C_{44}}. \end{aligned} \tag{10}$$

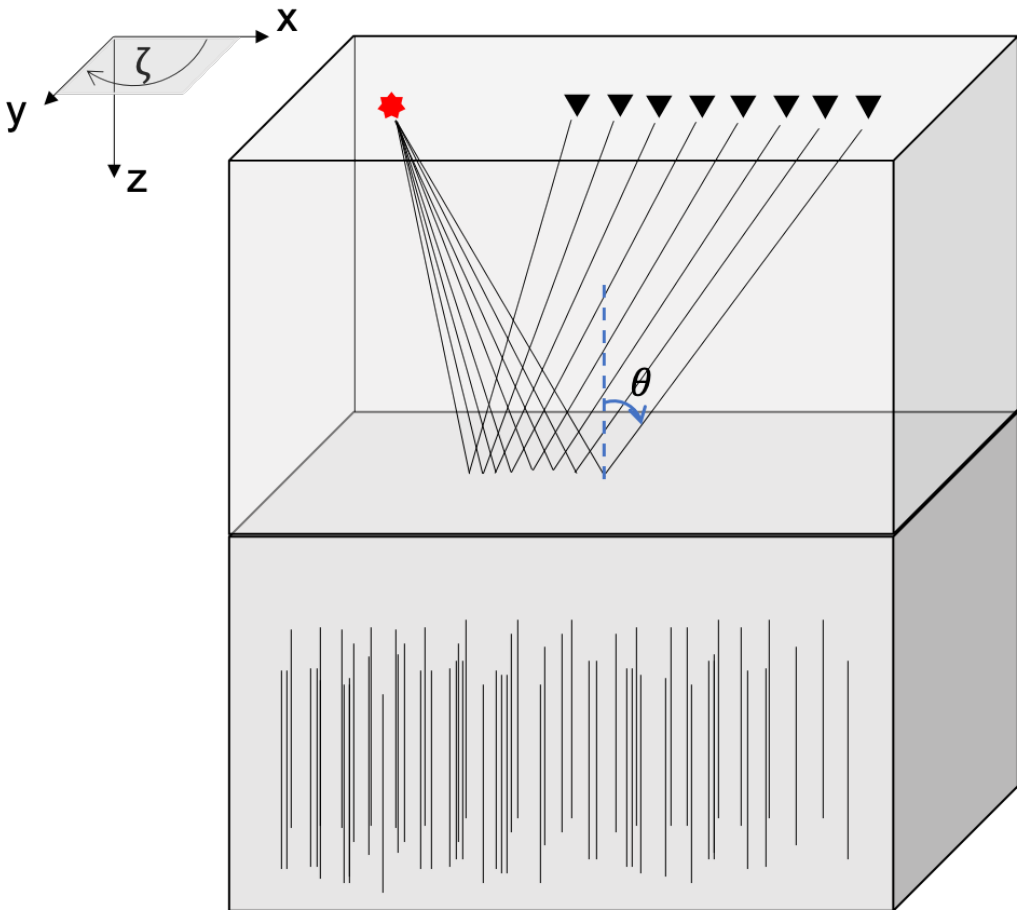

Figure 2: Schematic illustration of the AVOAz problem at the interface between an isotropic medium overlying a fractured HTI medium. θ and ζ symbolise the incidence and azimuthal angles, respectively. Fracture planes are perpendicular to the x-axis. The red star and the black triangles illustrate the locations of the source and receivers, respectively.

Lastly, $\Delta f = f_L - f_U$ and $\bar{f} = 1/2(f_L + f_U)$ denote the difference between and the average of the properties between the upper (subscript U) and lower (subscript L) media.

To study the poroelastic effects on the inversion of PP-wave reflection coefficient data, we consider three models for the fractured medium stiffness coefficients in Eq. 9: (i)

the "poroelastic model" with frequency-dependent C_{ij} coefficients; (ii) the low-frequency "elastic model" with real-valued C_{ij} coefficients corresponding to the relaxed limit of the "poroelastic model"; and (iii) the high-frequency "elastic model" which, correspondingly, represents the unrelaxed limit of the "poroelastic model".

INVERSE PROBLEM

In the previous section, we presented the forward problem consisting of modelling the AVOAz response of an interface between two HTI media. In the following, we provide a description of the Bayesian approach for solving the inverse problem as well as of the fractured rock properties that we attempt to retrieve from the AVOAz data.

Bayesian inversion

The general forward problem linking a set of model parameters of interest $\mathbf{m}_{true}$ to a set of observed data $\mathbf{d}_{obs}$ can be written as

$$\mathbf{d}_{obs} = F(\mathbf{m}_{true}) + \mathbf{e}_d, \tag{11}$$

where in this work $F(\cdot)$ is the forward modelling operator containing information about the physics and geometry of the ~~problem~~ AVOAz problem ($\mathbf{d}_{obs}$ is obtained from Eq. 9) and $\mathbf{e}_d$ denotes the noise associated with the measurement of the data. In general, for independent Gaussian noise the spread of the posterior distribution about the maximum value is controlled by e_d with larger e_d yielding broader likelihoods (e.g. Tarantola, 2005) . The corresponding inverse problem aims at estimating $\mathbf{m}_{true}$ from $\mathbf{d}_{obs}$, which generally requires knowledge of $F(\cdot)$ along with prior information with regard to the distribution of the parameters and errors. We formulate the inverse problem from a Bayesian point of view,

whereby a prior probability distribution for the parameters of interest $p(\mathbf{m})$ is updated to a posterior distribution based on the observed data $p(\mathbf{m}|\mathbf{d}_{obs})$ as follows ~~(e.g. Tarantola, 2005)~~ (e.g. Mosegaard ar

$$p(\mathbf{m}|\mathbf{d}_{obs}) = \frac{p(\mathbf{d}_{obs}|\mathbf{m})\, p(\mathbf{m})}{p(\mathbf{d}_{obs})}, \tag{12}$$

where $p(\mathbf{d}_{obs}|\mathbf{m})$ is the likelihood function and $p(\mathbf{d}_{obs})$ acts as a normalisation constant to ensure that the posterior distribution integrates to unity. Assuming independent and Gaussian distributed measurement errors with mean zero and standard deviation σ_d, the likelihood is described by

$$p(\mathbf{d}_{obs}|\mathbf{m}) = \frac{1}{(2\pi\sigma_d^2)^{N/2}} \exp\left[-\frac{||\mathbf{r}(\mathbf{m})||^2}{2\sigma_d^2}\right], \tag{13}$$

where $||\cdot||$ denotes the ℓ^2-norm and N is the number of data. The residual $\mathbf{r}(\mathbf{m})$ for some set of model paramaters is thus given by the sum of the parameter-error component and the Gaussian measurement noise $\mathbf{e}_d$

$$\begin{aligned} \mathbf{r}(\mathbf{m}) &= F(\mathbf{m}) - \mathbf{d}_{obs} \\ &= \underbrace{F(\mathbf{m}) - [F(\mathbf{m}_{true})}_{\substack{\text{parameter-error} \\ \text{component}}} + \mathbf{e}_d]. \end{aligned} \tag{14}$$

For $\mathbf{m} = \mathbf{m}_{true}$, the parameter-error component is zero and the likelihood function in Equation 13 will be maximised.

Equations 12 to 14 provide the necessary information to calculate the posterior probability of any parameter set $\mathbf{m}$. However, obtaining the statistical moments of the posterior distribution $p(\mathbf{m}|\mathbf{d}_{obs})$ often involves unfeasible multi-dimensional integrations. As a result, Markov-chain-Monte-Carlo (MCMC) methods are typically used to sample from $p(\mathbf{m}|\mathbf{d}_{obs})$ and quantify uncertainty in the inverse estimates (e.g., Tarantola, 2005). In this regard, we use the classical Metropolis-Hastings algorithm (e.g., Metropolis et al., 1953; Hastings, 1970), which has been described in detail in Köpke et al. (2018).

Model error

For the common scenario of using a simplified forward solver $\hat{F}(\mathbf{m})$ in the Bayesian inversion, the residual is given by the sum of a model-error component, a parameter-error component and the Gaussian measurement noise $\mathbf{e}_d$

$$\begin{aligned}\mathbf{r}(\mathbf{m}) &= \hat{F}(\mathbf{m}) - \mathbf{d}_{obs} \\ &= \hat{F}(\mathbf{m}) - [F(\mathbf{m}_{true}) + \mathbf{e}_d] \\ &= \underbrace{\hat{F}(\mathbf{m}) - F(\mathbf{m})}_{\substack{\text{model-error} \\ \text{component}}} + \underbrace{F(\mathbf{m}) - [F(\mathbf{m}_{true})}_{\substack{\text{parameter-error} \\ \text{component}}} + \mathbf{e}_d]. \end{aligned} \tag{15}$$

Comparing this result with Eq. 14 shows the addition of a model-error component, meaning that the likelihood function given in Equation 13 will not necessarily be maximised. Indeed, model error can lead to significant parameter biases and/or overconfident distributions if not adequately accounted for (Brynjarsdóttir and O'Hagan, 2014).

In this work, the detailed solver $F(\cdot)$ is given by a poroelastic model and we use this model to compute the "observed" data $\mathbf{d}_{obs}$. Model errors then arise when using a simplified solver $\hat{F}(\cdot)$ based on ~~an elastic model that considers either the~~ models neglecting poroelastic effects. In particular, we consider the model errors associated with the elastic high- ~~or~~ and the low-frequency limits of the underlying physical process.

Physical properties of fractured rocks

The properties characterising the fractured medium, for which we wish to invert using PP-wave reflection coefficient data, are the bulk modulus K_m, the shear modulus μ_m, the porosity ϕ of the background, the dry normal and tangential weaknesses due to the presence of the fractures Δ_N and Δ_T, respectively, and the volume fraction of fractures V_f. The dry

fracture weaknesses quantify the degree of fracturing of the rock and are related to the background medium properties as well as the dry fracture compliances of Eq. 3 (Bakulin et al., 2000)

$$\Delta_N = \frac{Z_N L_b}{(1 + Z_N L_b)}, \qquad \Delta_T = \frac{Z_T \mu_b}{(1 + Z_T \mu_b)}. \tag{16}$$

Weakness values range between 0 and 1, where 0 corresponds to an unfractured rock and 1 to an extreme degree of fracturing.

Given that the elastic models are not frequency-dependent, we cannot obtain any information on the background permeability ~~.~~ or the fracture intensity, which mainly affect the characteristic frequency of the mesoscopic WIFF (Eqs. 5 to 7). Hence, the background permeability in the fractured medium is assumed to be known and related to the porosity through the Kozeny-Carman relation for a packing of identical spheres of diameter d (e.g., Mavko et al., 2009)

$$\kappa = B \frac{\phi^3}{(1 - \phi^2)} d^2, \tag{17}$$

where B depends on the geometric characteristics of the pore space. Following Rubino et al. (2013), we chose B=0.003 and d=80 μm. The parameter H, on the other hand is set to 1 m, which means that fractures are separated 1 m. The grain and fluid properties are also assumed to be known and to be the same for the fractures and their embedding background.

Lastly, the porosity and permeability of open fractures are expected to be significantly higher than those of the embedding background. Fig. 3 shows that the P-wave modulus normal to the fractures is not sensitive to changes in porosity and permeability provided that they assume relatively high values. The lower limit for the fracture porosity was chosen based on the porosity values computed by Lissa et al. (2019) for synthetic open fractures having realistic aperture distributions. The permeability κ is constrained based

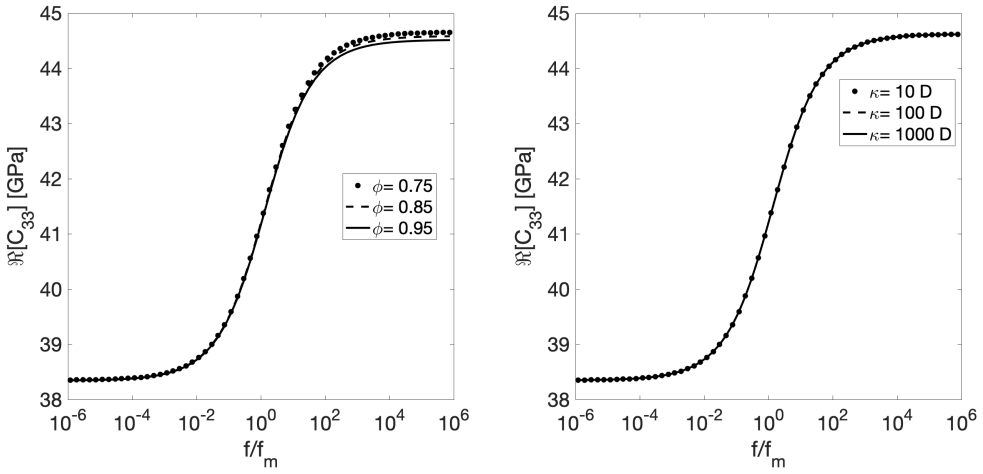

Figure 3: Sensitivity of the real component of the P-wave modulus normal to the fractures with regard to changes in fracture porosity ϕ and permeability κ. Maximum relative changes in $\Re[C_{33}]$ for varying porosity are $\sim$0.3%.

on the so-called cubic law, which predicts that for fractures with smooth walls separated by a uniform aperture h, we have $\kappa = h^2/12$ (Zimmerman and Main, 2004). For realistic apertures between 0.01 and 0.1 mm (Bakulin et al., 2000), fracture permeability is thus in the range between $\sim$10 and $\sim$1000 D. For our analysis, we assume that the porosity and permeability of the fractures are known and equal to 0.8 and 100 D, respectively. A summary of the properties is given in Table 1.

Isotropic medium properties

The elastic properties of the overlying isotropic medium correspond to those of a low-porosity sandstone and are given by (Pride, 2005)

$$\begin{aligned} K_m &= K_s \frac{1-\phi}{1+c\phi}, \\ \mu_m &= \mu_s \frac{1-\phi}{1+3c\phi/2}, \end{aligned} \tag{18}$$

where c is a parameter characterising the degree of consolidation between the solid grains and ranges between 2 (extremely consolidated) and 20 (poorly consolidated). In the following, we use $c = 5$. The porosity and permeability are 0.05 and 1μD, respectively. The properties of the upper medium are invariant throughout the analysis and the saturating fluid is the same as that of the fractured medium. Its seismic response is computed using the isotropic Gassmann (1951) equations. A summary of the properties is again provided by Table 1.

Inversion setup

To perform the forward modelling of the PP-wave reflection coefficients, we consider azimuthal angles $\zeta = \{0^\circ, 30^\circ, 60^\circ, 90^\circ\}$ and incidence angles θ from 0° to 50° discretised in steps of 1° (Fig. 2). For illustration purposes, the considered measurement frequency corresponds to the characteristic frequency f_m, at which seismic attenuation and velocity dispersion due to mesoscopic WIFF effects are maximal. Following Gurevich et al. (2009), this frequency is $f_m = 1/(2\pi\tau)$, with τ given by Eq. 6, and is equal to 131 Hz for the physical properties of the lower fractured medium given in Table 1. Note that by performing the analysis at $f = f_m$ the absolute error on the effective moduli predicted by both elastic models with respect to the poroelastic model is the same (Fig. 1).

Table 1: Physical properties employed in the inversion procedure.

Property	**Upper medium**	**Lower medium**
Dry frame bulk modulus K_m	28.12 GPa	13.5 GPa
Dry frame shear modulus μ_m	30.4 GPa	20 GPa
Grain bulk modulus K_s	37 GPa	37 GPa
Solid density ρ_s	2650 kg/m^3	2650 kg/m^3
Fluid density ρ_f	1090 kg/m^3	1090 kg/m^3
Fluid shear viscosity η_f	0.01 Poise	0.01 Poise
Fluid bulk modulus K_{fl}	2.25 GPa	2.25 GPa
Porosity ϕ	0.05	0.15
Grain shear modulus μ_s	44 GPa	–
Permeability κ	1μD	90.9 mD
Normal weakness Δ_N	–	0.2
Tangential weakness Δ_T	–	0.2
Fracture volume fraction V_f	–	0.001

To solve the inverse problem, we assume flat prior distributions for all model parameters whose minimum and maximum values are given in Table 2. We add uncorrelated Gaussian noise to the synthetic data with a standard deviation of $\sigma_d = 1 \times 10^{-3}$ and zero mean. For each MCMC inversion, we run one million iterations, of which the first 100,000 are discarded because they are regarded as representing the burn-in period.

	μ_m [GPa]	K_m [GPa]	Δ_N	Δ_T	ϕ	V_f
Synthetic truth $\mathbf{m}_{true}$	20	13.5	0.2	0.2	0.15	1E-3
Prior minimum	10	10	0.01	0.01	0.01	1E-4
Prior maximum	36	36	0.5	0.5	0.35	5E-3

Table 2: Prior ranges and true parameter values for the fractured medium.

RESULTS

Sensitivity analysis

Let us first consider the case in which we use the same forward solver in the inversion procedure as we did for generating "observed" synthetic data. This is also known as the "inverse crime" as the only error source is the Gaussian measurement noise. Nevertheless, this allows us to test the sensitivity of different forward solvers to each of the inverted parameters before introducing model errors into the inversion procedure. The synthetic data is generated using the parameter set $\mathbf{m}_{true}$ in Table 2. For the relaxed and unrelaxed models, this analysis represents the scenarios where the frequency of the seismic survey f_{surv} is expected to be much higher or much lower than f_m, respectively.

The data are PP-wave reflection coefficients as functions of the angles ζ and θ at a single frequency equal to f_m, which gives a total of 204 data points. Fig. 4 shows the inversion results when using the two elastic models as well as the poroelastic model. For all models, accurate estimates are obtained for the elastic moduli of the background μ_m and K_m and the tangential weakness Δ_T. The posterior distributions for the porosity ϕ are narrow for all models but that corresponding to the high-frequency elastic model is biased. The normal weakness Δ_N exhibits a decreasing sensitivity (broader posterior distribution) as the model approaches the unrelaxed limit. The decrease in sensitivity is related to the fact that, as the fractures tend to be more hydraulically isolated from the embedding background, their response becomes dominated by their saturating fluid instead of their dry elastic properties (Brajanovski et al., 2005). Lastly, the fracture volume fraction V_f is not satisfactorily resolved by any of the models. At low frequencies, on the other hand, both the excess porosity in the medium due to the presence of the fractures $V_f\phi_f$ and the background porosity ϕ_b contribute to the fluid-related stiffening effect on the saturated effective moduli. Since $\phi_b \gg V_f\phi_f$, the sensitivity of the seismic response of the medium to the fracture porosity effect is expected to be negligible in the relaxed limit. At high frequencies, the fractures and their embedding background behave as being hydraulically isolated and only the porosity of the fractures contributes to the fluid-related stiffening effects in the fractures. An increased sensitivity of the seismic response to $V_f\phi_f$ is thus expected for the high-frequency solution. In this context, one of the advantages of the model of Guo et al. (2017a,b) is that it accounts for the effects associated with the finite aperture of the fractures. In spite of this, the sensitivity to V_f under unrelaxed conditions is not good enough to allow for its inversion from PP-wave data.

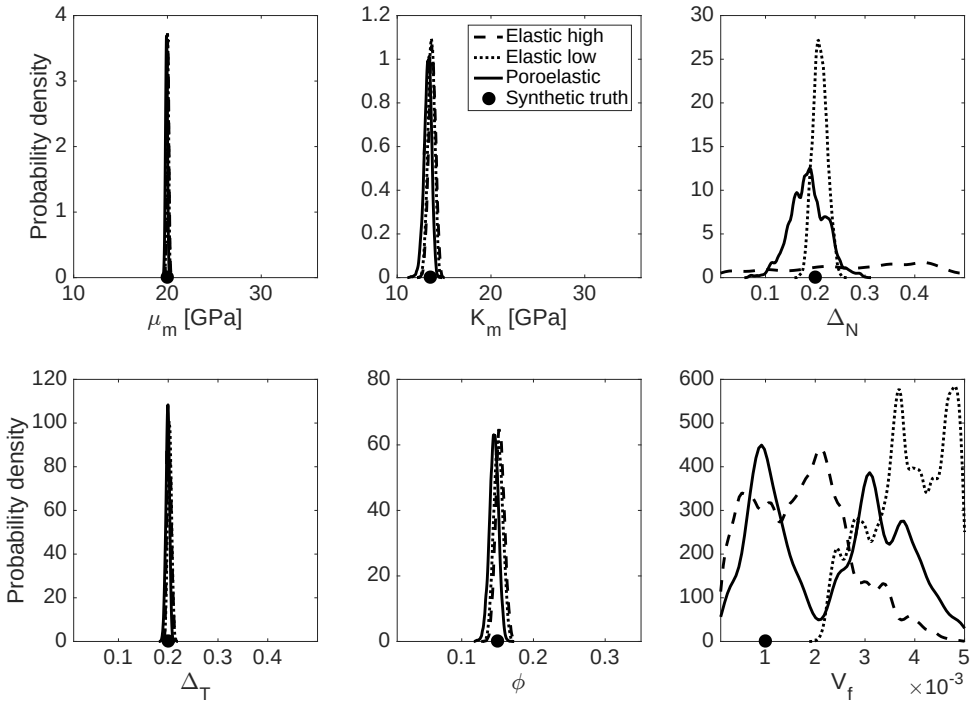

Figure 4: Inversion results obtained in the case of no model error. That is, we use the same model to generate the synthetic reflection coefficient data as for the inversion thereof. Three effective medium models are considered: poroelastic (solid curve), low-frequency elastic (dotted curve), and high-frequency elastic (dashed curve). Dots denote the "true" parameter values.

Model error analysis

Next, we consider the case in which the synthetic data are generated using the poroelastic model with the "true" parameter set, whereas the elastic models are used as forward solvers in the inversion process. We wish to analyse the resulting bias with regard to the posterior distributions due to model error. The PP-wave reflection data distribution is the same as

in the preceding sensitivity analysis.

The corresponding results are shown in Fig. 5. We observe that, overall, the relaxed elastic model provides better estimations compared to its unrelaxed counterpart when the data are affected by WIFF effects. The shear modulus of the background ~~is~~ and tangential weakness are very well constrained by both models, implying that ~~this property~~ these properties can be correctly estimated regardless of frequency-dependent effects. Similarly, the bulk modulus is well constrained by both models, albeit slightly better for the elastic low-frequency approximation. The results obtained for the normal weakness of the medium show an interesting behavior as the posterior distribution of the low-frequency model is well defined but biased towards lower values. This underestimation is related to the fact that the influence of Δ_N on the effective seismic properties is maximal at low-frequencies. Hence, lower values of Δ_N are needed to explain the effective stiffness of the medium when the stiffening effect due to WIFF is not taken into account. The high-frequency elastic model, on the other hand, has no sensitivity to the normal weakness, which is expected from the analysis shown in Fig. 4. Also expected is that the fracture volume fraction is poorly resolved in both cases. ~~The low-frequency model provides a better estimate of V_f, although at low frequencies the sensitivity to V_f is expected to be minimal.~~ Regarding the porosity~~and tangential weakness~~, the effects of neglecting the frequency dependence affects the inversion based on an unrelaxed elastic model more prominently than the one based on the relaxed model. For ~~both properties~~this property, the posterior ~~distributions are~~ distribution is well defined but slightly biased.

From the analysis of Figs. 4 and 5 it follows that the inversion performance strongly depends on the forward model selection. ~~In~~ It is important to remark that in Fig. 5, we assume that the frequency of the seismic survey f_{surv} is close to the characteristic frequency

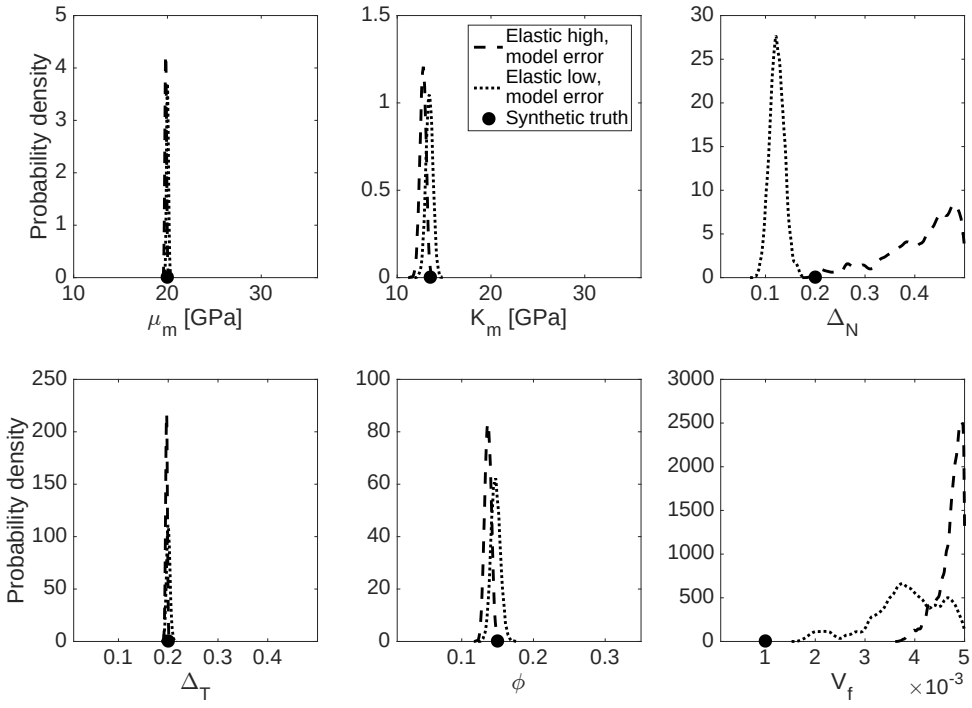

Figure 5: Inversion results with model error. The poroelastic model is used to generate the synthetic data, while the low- (dotted curve) and high-frequency elastic models (dashed curve) are employed for the inversion. Dots denote the "true" parameter values. Note that the inversion of the fracture volume fraction V_f with the high-frequency model gives a peak at around $7{\times}10^{-3}$ when considering a larger range of prior values.

f_m, at which mesoscopic WIFF effects are maximal. Although for brevity we only show results for the subsurface model given by the properties of Table 1, our results can be used to infer the elastic modelling performance in other scenarios. When f_{surv} is expected to be lower than f_m, which is typically the case for high background permeability or low fracture density, the performance of the relaxed elastic model will lie somewhere between the results

shown in Figs. 4 and 5. The same conclusion holds when f_{surv} is expected to be higher than f_m, which is the case for a low background permeability or high fracture density, with regard to the performance of the unrelaxed elastic model in the AVOAz inversion.

Frequency-dependent data

From the analysis of Figs. 4 and 5, we can conclude that the use of elastic models may, even in the absence of model error, result in highly confident but biased inversion results. Interestingly, our sensitivity analysis shows that a poroelastic model does not produce acceptable results for V_f and Δ_N (Fig. 4). Given that the effective properties of a fluid-saturated fractured medium are frequency-dependent, we now test the impact of considering a frequency-dependent data set. We assume a frequency range such that $f/f_m = \{0.76, 1.21, 1.91, 3.03, 4.81, 7.63\}$, which results in 1224 data points. Note that for the characteristic frequency given by the properties in Table 1, the frequency range spans from 100 to 1000 Hz. However, the inversion results are the same regardless of the absolute frequency values as long as the ratio with respect to f_m remains the same.

Fig. 6 shows the case of an inversion using the poroelastic model without model error. We do not consider elastic models as they neglect frequency-dependent effects. We compare the inversion results for a single-frequency data set (solid curve in Fig. 6, which is equal to that in Fig. 4) and a frequency-dependent data set (dashed curve). The impact of considering frequency-dependent data is not negligible, as all properties are better constrained by the inversion and the improvement is substantial with respect to the normal weakness as well as the fracture volume fraction. In general, additional information with regard to the dispersion of the stiffness of the fractured medium (Fig. 1) allows for more accurate

description of those fracture properties influencing WIFF effects.

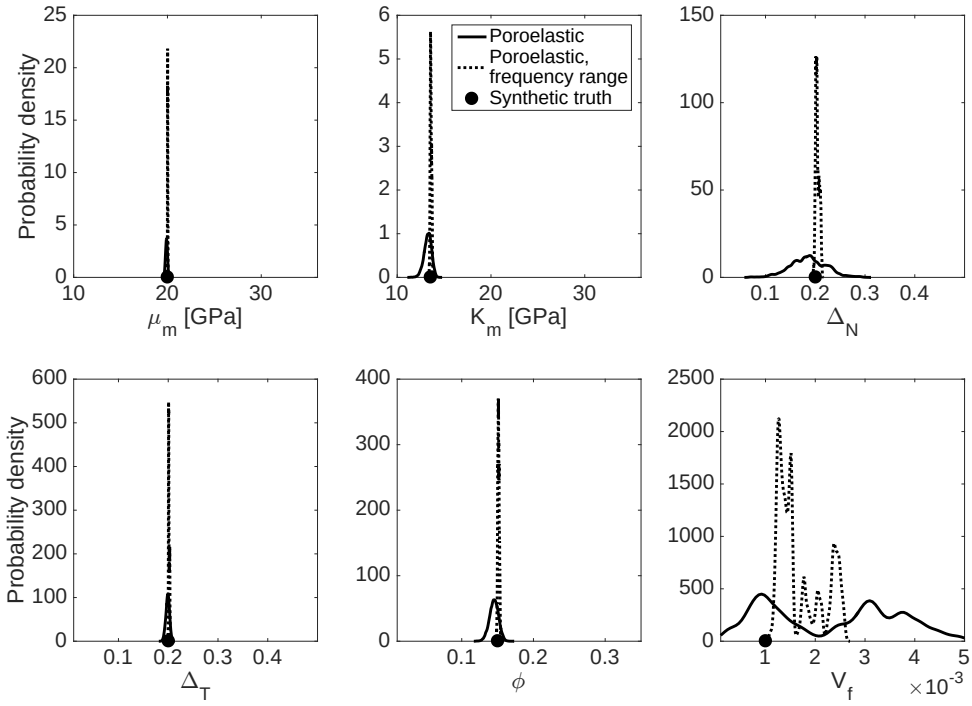

Figure 6: Inversion results without model error considering the poroelastic model to generate the synthetic reflection coefficient data as well as for the inversion. The solid curve corresponds to an inversion considering only a single frequency, while the dashed curve corresponds to a frequency-dependent data set. Dots denote the "true" parameter values.

DISCUSSION

Use of Rüger's (1998) approximation

Exact reflection coefficients can be computed by numerically solving the linear system of equations resulting from imposing the continuity of stress and displacements across the

interface (e.g., Carcione, 1997). Behura and Tsvankin (2009) showed that for an incident P-wave with a zero inhomogeneity angle (the angle between the real and imaginary parts of the wave vector), the form of the PP- and the PS-wave reflection coefficients in arbitrarily anisotropic viscoelastic media is the same as in purely elastic media, but all terms become complex-valued and frequency-dependent. In practice, simple analytical approximations based on the assumption of weak anisotropy, such as that given by Eq. 9 (Rüger, 1998) tend to be used. Fig. 7 shows that this indeed provide a very good approximation of Carcione's (1997) exact solution of the reflectivity problem over a wide range of incidence angles and hence is fully adequate for the purpose of this study. Please note that, we only consider the reflection coefficients for $\zeta = 0^\circ$ due to the 2D nature of the exact solution.

Anisotropy of fractured medium

The scenario of a fractured medium with HTI symmetry is favourable for our inversion setup as the reflection coefficients vary both with azimuth ζ and incidence angle θ. The inversion results are expected to be worse when the sensitivity to any of these two angles decreases. To illustrate this, we consider a fractured VTI medium, for which the symmetry axis is parallel to z-direction and the data only vary with θ. The corresponding expressions for the reflection coefficients are given in Appendix B. The stiffness matrix describing the VTI medium can be obtained by performing a 90° rotation of the matrix corresponding to the HTI medium (e.g., Mavko et al., 2009).

As for the HTI case, we consider PP-wave reflection coefficient data at a single frequency equal to f_m. As the data only depend on θ, the number of data points reduces to 51. Fig. 8 shows a sensitivity analysis similar to the one shown in Fig. 4 where the same

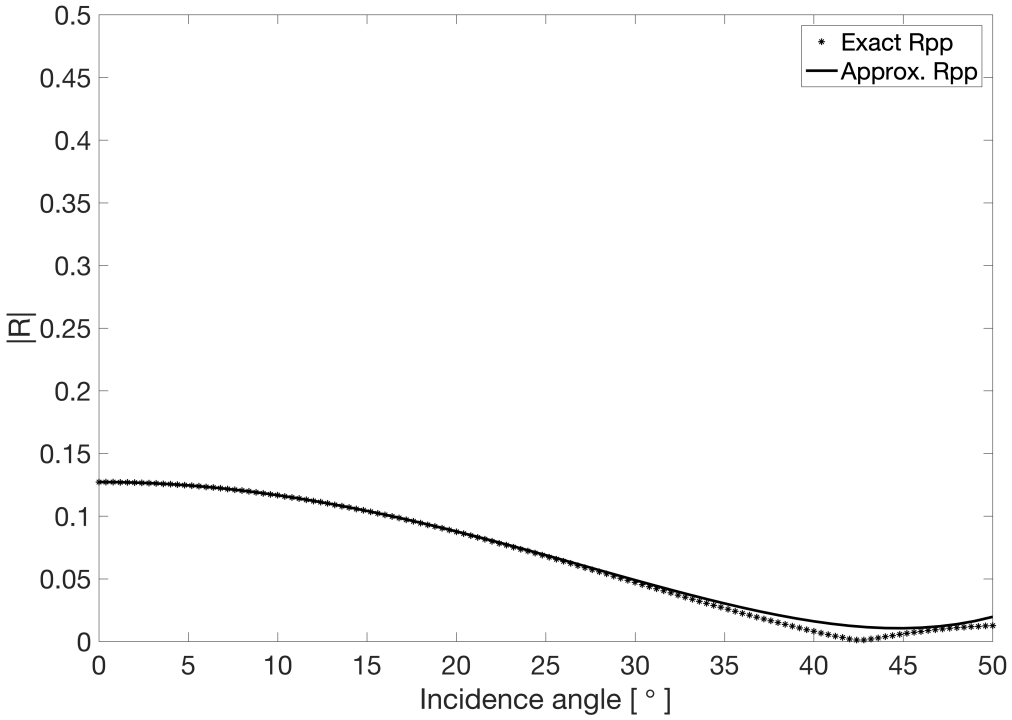

Figure 7: Comparison of reflection coefficients computed using the exact solution of Carcione (1997) (dots) and the approximate solution of Rüger (1998) (solid curve) for $\zeta = 0°$. The interface separates an elastic isotropic medium overlying a viscoelastic HTI medium. The physical properties of the model are given in Table 1.

model is utilised in the inversion and in the forward solver to generate the "observed" data. Compared with the HTI case, the results are clearly worse. The sensitivity of the reflection coefficients to Δ_N, Δ_T, and V_f is very poor. The results for the elastic moduli of the background are acceptable. As opposed to the HTI case, the background porosity results are poorest for the low-frequency elastic model. The case with model error is not shown because, based on the above sensitivity analysis, the performance of the inversion procedure

is expected to be extremely poor.

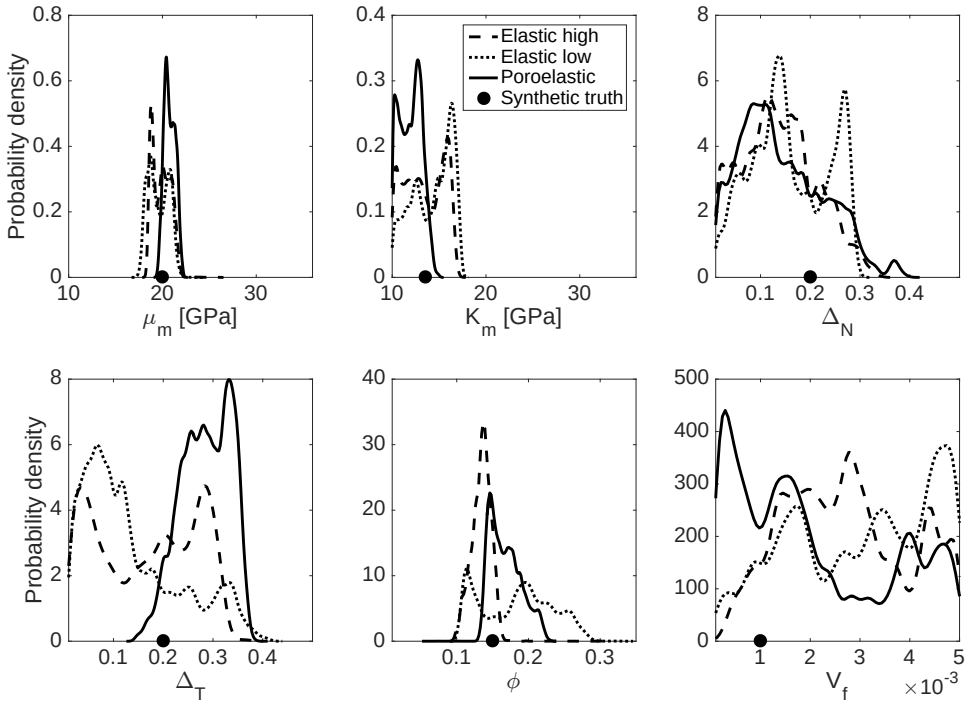

Figure 8: Inversion results without model error for a fractured VTI medium overlain by an isotropic elastic medium. Only PP-wave reflection coefficients are considered. Three effective medium models are considered, namely, the poroelastic (solid curve), low-frequency elastic (dotted curve), and the high-frequency elastic model (dashed curve). Dots denote the "true" parameter values given in Table 1.

In an attempt to improve the inversion results shown in Fig. 8, we have considered frequency-dependent reflection coefficient data. The additional data correspond to the same frequency range considered for the HTI case. Fig. 9 shows the corresponding results. In general, the frequency-dependent data provide better results than the single-frequency data. The background properties are better constrained and, as for the HTI case, there is

a slight improvement with regard to the normal weakness results. However, the inherent lack of sensitivity to fracture properties due to the symmetry of the fractured medium also persists for the frequency-dependent data.

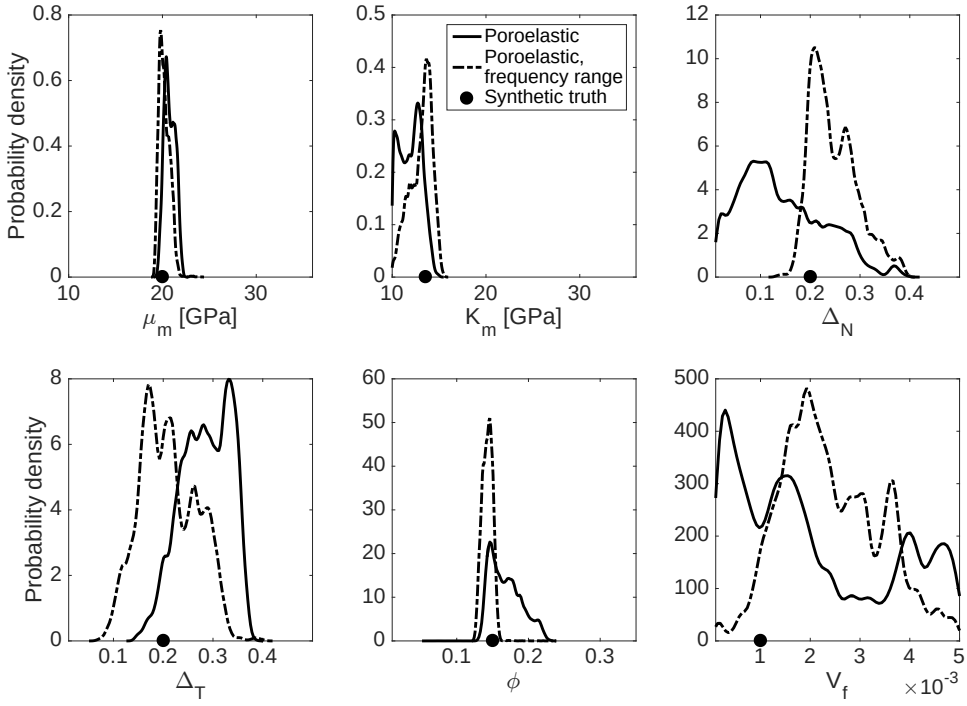

Figure 9: Inversion results without model error considering the poroelastic model to both generate and invert the synthetic reflection coefficient data. The solid curve corresponds to an inversion considering only a single frequency, while the dashed curve represents a frequency-dependent data set. Dots denote the "true" parameter values.

Inverse problem

This work was focused on the inversion of reflectivity characteristics, because reflection coefficients are commonly estimated in seismic reflection experiments and the approximations

considered in this study are broadly accepted in the community. We have, however, also explored the inversion of phase velocity anisotropy data. The results related to the model error were similar to those shown in this work. That is, the main error was observed in the estimation of the normal weakness Δ_N. In this work, we have assumed the saturating fluid to be known. Future studies can include the fluid properties into the inversion procedure. Moreover, a partial fluid saturation can be accounted for and quantified through a saturation parameter. Note that for lower bulk modulus of the fluid (e.g., gas-saturated fractures), the pressure gradients induced by the waves are less significant and, correspondingly, the magnitude of the associated poroelastic effects decreases. In this case, an elastic model is expected to perform better than in a fully water-saturated case. On the other hand, we can see that the viscosity of the fluid affects the characteristic frequency of the mesoscopic WIFF. More realistic fracture distributions, such as random distributions, can be considered by using numerical simulations instead of analytical models, from which the elastic models can be obtained from the low- and high-frequency limits of the poroelastic solution. However, for expensive forward solvers of this kind, the inversion scheme considered in this study is not be feasible, as obtaining meaningful statistics with MCMC often requires millions of iterations. One approach for circumventing this problem involves the analysis and correction for the model error, which may reduce the bias of the posterior parameter distribution (e.g., Köpke et al., 2018).

CONCLUSIONS

We have explored the impact of neglecting mesoscopic WIFF effects in the inversion of fractured rock properties from seismic reflection coefficient data. We have considered a poroelastic model to describe the frequency-dependent anisotropic seismic response of a

medium containing parallel fractures with HTI symmetry. The model error is introduced by considering elastic models in the inversion procedure, which correspond to the typically used relaxed and unrelaxed limits of the underlying poroelastic model. We have chosen the properties of the fractured medium in such a way that WIFF effects related to the poroelastic nature of the underlying model are maximal at the frequency of the data. The inverse problem consists of estimating both fracture and background rock properties from PP-wave reflection coefficients observed at different azimuths and incidence angles.

An initial sensitivity analysis showed that even when the assumptions of the elastic models are fulfilled, errors in the estimation of the fracture volume fraction as well as significant uncertainties in the degree of fracturing are expected. When WIFF effects are included in the synthetic data, a relaxed, Gassmann-type elastic model provides better inversion results than the unrelaxed model, which assumes hydraulically isolated fractures. While the unrelaxed elastic model cannot resolve the degree of fracturing, the relaxed model provides a well-defined but biased posterior distribution, which underestimates the degree of fracturing. We have shown that the sensitivity of the poroelastic model to the fracture volume fraction and the normal weakness is weak when considering single-frequency data. Conversely, the use of frequency-dependent data in the inversion procedure significantly improves the corresponding estimations.

ACKNOWLEDGMENTS

Part of this work was completed within the Swiss Competence Center for Energy Research-Supply of Electricity with support of Innosuisse and from the Swiss National Sciences Foundation through grants no 149240 and 200021-140864.

APPENDIX A: EFFECTIVE PROPERTIES OF FLUID-SATURATED FRACTURED ROCKS

Relaxed regime

Gassmann's (1951) anisotropic equations allow to compute the relaxed or low-frequency limit of the effective stiffness matrix of the fluid-saturated rock. The corresponding C_{ij}^r elements are related to the dry-frame stiffness coefficients C_{ij}^{dry} as

$$C_{ij}^r = C_{ij}^{dry} + \alpha_i \alpha_j M \qquad i,j = 1,...,6. \tag{A-1}$$

The coefficients α_m are

$$\alpha_m = 1 - \frac{\sum_{n=1}^{3} C_{mn}^{dry}}{3K_g} \qquad m = 1,2,3, \tag{A-2}$$

$\alpha_4 = \alpha_5 = \alpha_6 = 0$, and the scalar M is

$$M = \frac{K_g}{(1 - \frac{K^*}{K_g}) - \phi(1 - \frac{K_g}{K_{fl}})}. \tag{A-3}$$

In Eqs. A-1 to A-3, ϕ is the overall porosity of the fractured rock, which includes the porosities of the background and the fractures. The latter is equal to $V_f \phi_f$ where ϕ_f the porosity of the fracture infill material. In addition, K_g denotes the grain solid bulk modulus, K_{fl} the pore fluid bulk modulus, and K^* the generalised drained bulk modulus defined as

$$K^* = \frac{1}{9} \sum_{i=1}^{3} \sum_{j=1}^{3} C_{ij}^{dry}. \tag{A-4}$$

In the following, we refer to the elastic model defined by the stiffness coefficients C_{ij}^r as the low-frequency elastic model.

Unrelaxed regime

Guo et al. (2017a) showed that it is possible to obtain the stiffness coefficients in the high-

frequency or unrelaxed regime from the properties of the dry rock by proceeding in a similar way as for the relaxed regime. Given that fractures behave as being hydraulically isolated, we first compute the effective properties corresponding to the dry fractures embedded in a saturated background

$$\mathbf{C}_1 = (\mathbf{S}_1)^{-1} = (\mathbf{S}_b^{\text{sat}} + \mathbf{Z}^{\text{dry}})^{-1} \quad , \tag{A-5}$$

where the elements of the compliance matrix of the saturated background $\mathbf{S}_b^{\text{sat}}$ are computed using the isotropic Gassmann (1951) equations. Next, we proceed, as for the relaxed limit, to saturate the fractures. To do so, we consider Eqs. A-1 to A-4 but using $\mathbf{C}_1$ instead of $\mathbf{C}^{\text{dry}}$, the saturated bulk modulus $K_m^{\text{sat}} = K_m + \alpha^2 M$ of the isotropic background instead of the solid grains bulk modulus K_g, and the fracture porosity instead of the overall porosity, ϕ. K_m, α, and M are the bulk modulus of the dry matrix, the Biot-Willis coefficient and the pore space modulus, respectively. The thus obtained coefficients correspond to those of the unrelaxed stiffness matrix C_{ij}^u. We refer to the elastic model defined by the C_{ij}^u coefficients as the high-frequency elastic model.

APPENDIX B: REFLECTION COEFFICIENTS FOR VTI MEDIA

Here, we present the equations necessary to compute the reflectivity of an interface separating two VTI media for P-wave incidence. Following Mavko et al. (2009), the PP-wave reflection coefficient for weakly anisotropic VTI media in the limit of small impedance contrast is

$$R_{PP}(\theta) = \frac{\Delta Z}{2\bar{Z}} + \frac{1}{2}\left[\frac{\Delta\alpha}{\bar{\alpha}} - \left(\frac{2\bar{\beta}}{\bar{\alpha}}\right)^2 \frac{\Delta G}{\bar{G}} + \Delta\delta\right]\sin^2(\theta) + \frac{1}{2}\left[\frac{\Delta\alpha}{\bar{\alpha}} + \Delta\varepsilon\right]\sin^2(\theta)\tan^2(\theta), \tag{A-6}$$

with α, β, G, Z, ε given in Eq. 10 and

$$\delta = \frac{(C_{13} + C_{44})^2 - (C_{33} - C_{44})^2}{2C_{33}(C_{33} - C_{44})}. \tag{A-7}$$

For completeness, we also show the corresponding PS-reflection coefficient although it is not needed for the purpose of this study. Please note that the corresponding expressions in Mavko et al. (2009) are subject to some typographic errors, which have been corrected here

$$\begin{aligned} R_{PS}(\theta) = &-\frac{\Delta\rho}{2\bar{\rho}}\frac{\sin(\theta)}{\cos(\theta_s)} - \frac{\bar{\beta}}{\bar{\alpha}}\left(\frac{2\Delta\beta}{\bar{\beta}} + \frac{\Delta\rho}{\bar{\rho}}\right)\sin(\theta)\cos(\theta) + \left(\frac{\bar{\beta}}{\bar{\alpha}}\right)^2\left(\frac{2\Delta\beta}{\bar{\beta}} + \frac{\Delta\rho}{\bar{\rho}}\right)\frac{\sin^3(\theta)}{\cos(\theta_s)} + \\ &\left[\left(\frac{\bar{\alpha}^2}{2(\bar{\alpha}^2 - \bar{\beta}^2)\cos(\theta_s)} - \frac{\bar{\alpha}\bar{\beta}\cos(\theta)}{2(\bar{\alpha}^2 - \bar{\beta}^2)}\right)\Delta\delta\right]\sin(\theta) + \left[\frac{\bar{\alpha}\bar{\beta}\cos(\theta)}{(\bar{\alpha}^2 - \bar{\beta}^2)}(\Delta\delta - \Delta\varepsilon)\right]\sin^3(\theta) - \\ &\left[\frac{\bar{\alpha}^2}{(\bar{\alpha}^2 - \bar{\beta}^2)\cos(\theta_s)}(\Delta\delta - \Delta\varepsilon)\right]\sin^3(\theta) + \left[\frac{\bar{\beta}^2}{2(\bar{\alpha}^2 - \bar{\beta}^2)\cos(\theta_s)}\Delta\delta\right]\sin^3(\theta) + \\ &\left[\frac{\bar{\beta}^2}{(\bar{\alpha}^2 - \bar{\beta}^2)\cos(\theta_s)}(\Delta\delta - \Delta\varepsilon)\right]\sin^5(\theta). \end{aligned} \tag{A-8}$$

REFERENCES

Al-Harrasi, O., J.-M. Kendall, and M. Chapman, 2011, Fracture characterization using frequency-dependent shear wave anisotropy analysis of microseismic data: Geophysical Journal International, **185**, 1059–1070.

Ali, A., and M. Jakobsen, 2014, Anisotropic permeability in fractured reservoirs from frequency-dependent seismic amplitude versus angle and azimuth data: Geophysical Prospecting, **62**, 293–314.

Bakulin, A., V. Grechka, and I. Tsvankin, 2000, Estimation of fracture parameters from reflection seismic data—part I: HTI model due to a single fracture set: Geophysics, **65**, 1788–1802.

Barbosa, N. D., J. G. Rubino, E. Caspari, and K. Holliger, 2018, Impact of fracture clustering on the seismic signatures of porous rocks containing aligned fractures: Geophysics, **83**, 1–54.

Behura, J., and I. Tsvankin, 2009, Reflection coefficients in attenuative anisotropic media: Geophysics, **74**, WB193–WB202.

Brajanovski, M., B. Gurevich, and M. Schoenberg, 2005, A model for P-wave attenuation and dispersion in a porous medium permeated by aligned fractures: Geophysical Journal International, **163**, 372–384.

Brynjarsdóttir, J., and A. O'Hagan, 2014, Learning about physical parameters: The importance of model discrepancy: Inverse Problems, **30**, 114007.

Carcione, J. M., 1997, Reflection and transmission of qp-qs plane waves at a plane boundary between viscoelastic transversely isotropic media: Geophysical Journal International, **129**, 669–680.

Chapman, M., 2003, Frequency-dependent anisotropy due to meso-scale fractures in the

presence of equant porosity: Geophysical Prospecting, **51**, 369–379.

Chapman, M., E. Liu, and X.-Y. Li, 2006, The influence of fluid sensitive dispersion and attenuation on AVO analysis: Geophysical Journal International, **167**, 89–105.

Chen, H., Y. Ji, and K. A. Innanen, 2017, Estimation of modified fluid factor and dry fracture weaknesses using azimuthal elastic impedance: Geophysics, **83**, WA73–WA88.

Downton, J. E., 2005, Seismic parameter estimation from avo inversion: University of Calgary, Department of Geology and Geophysics.

Fang, X., Y. Zheng, and M. C. Fehler, 2016, Fracture clustering effect on amplitude variation with offset and azimuth analyses: Geophysics, **82**, N13–N25.

Gassmann, F., 1951, Über die elastizität poröser medien: Vierteljahresschrift der Naturforschenden Gesellschaft in Zürich, **96**.

Guo, J., J. G. Rubino, N. D. Barbosa, S. Glubokovskikh, and B. Gurevich, 2017a, Seismic dispersion and attenuation in saturated porous rocks with aligned fractures of finite thickness: Theory and numerical simulations – Part I: P-wave perpendicular to the fracture plane: Geophysics, **83**, WA49–WA62.

———, 2017b, Seismic dispersion and attenuation in saturated porous rocks with aligned fractures of finite thickness: Theory and numerical simulations – Part II: Frequency-dependent anisotropy: Geophysics, **83**, WA63–WA71.

Gurevich, B., M. Brajanovski, R. J. Galvin, T. M. Müller, and J. Toms-Stewart, 2009, P-wave dispersion and attenuation in fractured and porous reservoirs–poroelasticity approach: Geophysical Prospecting, **57**, 225–237.

Hastings, W. K., 1970, Monte Carlo sampling methods using Markov chains and their applications: Biometrika, **57**, 97–109.

Hudson, J. A., 1980, Overall properties of a cracked solid: Mathematical Proceedings of the

Cambridge Philosophical Society, Cambridge University Press, 371–384.

Köpke, C., J. Irving, and A. H. Elsheikh, 2018, Accounting for model error in bayesian solutions to hydrogeophysical inverse problems using a local basis approach: Advances in Water Resources, **116**, 195–207.

Krzikalla, F., and T. M. Müller, 2011, Anisotropic P-SV-wave dispersion and attenuation due to inter-layer flow in thinly layered porous rocks: Geophysics, **76**, WA135–WA145.

Liu, E., and A. Martinez, 2013, Seismic fracture characterization: Concepts and practical applications: EAGE.

Maultzsch, S., M. Chapman, E. Liu, and X. Y. Li, 2003, Modelling frequency-dependent seismic anisotropy in fluid-saturated rock with aligned fractures: implication of fracture size estimation from anisotropic measurements: Geophysical Prospecting, **51**, 381–392.

———, 2007, Modelling and analysis of attenuation anisotropy in multi-azimuth VSP data from the Clair field: Geophysical Prospecting, **55**, 627–642.

Mavko, G., T. Mukerji, and J. Dvorkin, 2009, The rock physics handbook: Tools for seismic analysis of porous media: Cambridge university press.

Metropolis, N., A. W. Rosenbluth, M. N. Rosenbluth, A. H. Teller, and E. Teller, 1953, Equation of state calculations by fast computing machines: The Journal of Chemical Physics, **21**, 1087–1092.

Mosegaard, K., and A. Tarantola, 1995, Monte Carlo sampling of solutions to inverse problems: Journal of Geophysical Research: Solid Earth, **100**, 12431–12447.

Müller, T. M., B. Gurevich, and M. Lebedev, 2010, Seismic wave attenuation and dispersion resulting from wave-induced flow in porous rocks—a review: Geophysics, **75**, 75A147–75A164.

National Research Council, 1996, Rock fractures and fluid flow: contemporary understand-

ing and applications: National Academies Press.

Pride, S. R., 2005, Relationships between seismic and hydrological properties, *in* Hydrogeophysics: Springer, 253–290.

Rathore, J., E. Fjaer, R. Holt, and L. Renlie, 1995, P-and S-wave anisotropy of a synthetic sandstone with controlled crack geometry: Geophysical Prospecting, **43**, 711–728.

Rubino, J. G., L. B. Monachesi, T. M. Müller, L. Guarracino, and K. Holliger, 2013, Seismic wave attenuation and dispersion due to wave-induced fluid flow in rocks with strong permeability fluctuations: The Journal of the Acoustical Society of America, **134**, 4742–4751.

Rüger, A., 1998, Variation of p-wave reflectivity with offset and azimuth in anisotropic media: Geophysics, **63**, 935–947.

———, 2002, Reflection coefficients and azimuthal avo analysis in anisotropic media: Society of Exploration Geophysicists.

Schoenberg, M., 1980, Elastic wave behavior across linear slip interfaces: The Journal of the Acoustical Society of America, **68**, 1516–1521.

Schoenberg, M., and J. Douma, 1988, Elastic wave propagation in media with parallel fractures and aligned cracks: Geophysical Prospecting, **36**, 571–590.

Schoenberg, M., and C. M. Sayers, 1995, Seismic anisotropy of fractured rock: Geophysics, **60**, 204–211.

Shen, F., J. Sierra, D. R. Burns, and M. N. Toksöz, 2002, Azimuthal offset-dependent attributes applied to fracture detection in a carbonate reservoir: Geophysics, **67**, 355–364.

Tarantola, A., 2005, Inverse problem theory and methods for model parameter estimation: SIAM.

Thomsen, L., 1995, Elastic anisotropy due to aligned cracks in porous rock: Geophysical Prospecting, **43**, 805–829.

Tillotson, P., M. Chapman, A. I. Best, J. Sothcott, C. McCann, W. Shangxu, and X.-Y. Li, 2011, Observations of fluid-dependent shear-wave splitting in synthetic porous rocks with aligned penny-shaped fractures: Geophysical Prospecting, **59**, 111–119.

Tillotson, P., M. Chapman, J. Sothcott, A. I. Best, and X.-Y. Li, 2014, Pore fluid viscosity effects on P- and S-wave anisotropy in synthetic silica-cemented sandstone with aligned fractures: Geophysical Prospecting, **62**, 1238–1252.

Zimmerman, R., and I. Main, 2004, Hydromechanical behavior of fractured rocks: International Geophysics Series, **89**, 363–422.